# Numerical Simulation of Lubricant Migration

# on the Flying Head Slider Surface in Hard Disk Drives

Hiroyuki Kubotera
Visiting industrial fellow
Department of Mechanical Engineering
University of California at Berkeley
kubotera@cml.me.berkeley.edu


David B. Bogy
William S. Floyd, Jr. Distinguished Professor in Engineering
Department of Mechanical Engineering
University of California at Berkeley
dbogy@cml.me.berkeley.edu

INDEX

1.  Abstract

In this paper we numerically study lubricant migration on a flying slider air bearing surface in a hard disk drive. Based on the continuum thin film lubrication theory with inter-molecular forces and a precursor film model, we develop a lubricant migration solver. Our numerical simulation model includes air bearing pressure, air bearing shear stress, Laplace pressure, the dispersive and polar components of the surface free energy, the dispersive and polar components of the disjoining pressure and the shear stress caused by the surface free energy gradient. Using the newly developed solver we investigate the detailed lubricant migration behavior on a modern negative pressure type slider surface. We find distinct lubricant migration speeds, mainly depending on the etch depth of the slider surfaces and the accumulation of lubricant at specific regions. We find that the lubricant migration behavior largely correlates with the magnitude and direction of the air bearing shear stress. Moreover we reveal the contributions of the various physical models to the lubricant migration. We find that the air bearing shear stress has a dominant effect on the lubricant profile evolution and the disjoining pressure also affects the lubricant evolution through diffusion. By contrast, the air bearing pressure and the Laplace pressure have minor effects on the lubricant thickness evolution. We also study the contribution of the oscillatory polar component of the disjoining pressure, and we find that it causes multiple small lubricant droplets to emerge on the slider surface. We further demonstrate the lubricant migration on various different slider designs and flying conditions. We find that the slider design and flying condition largely affect the lubricant migration pattern.

2.  Introduction

In order to achieve higher recording densities in hard disk drives, ultra-low flying height of the flying head slider is required. Recently the flying height in hard disk drive products

has been reduced to less than 10nm. In such an ultra-low flying height region the probability of contact between the flying slider and the disk is high. During such contact the lubricant on the disk will transfer droplets to the slider, and they migrate along its surface due to several forces. These lubricant droplets can cause flying height changes and they could lead to a head crash in the worst case. Therefore the lubricant flow behavior on the flying head slider is important in ultra-low flying height regions of the slider.

 Recently Wu [1] and Zhang et al. [2] performed lubricant flow simulations on slider surfaces. However the slider designs used in their lubricant flow simulations are relatively simple and the contributions of the various related physical models are still not well understood. In this paper we develop a lubricant migration solver on the slider surface and investigate the detailed lubricant behavior for a modern negative pressure type slider surface. In addition, in order to obtain useful knowledge for designing ultra-low flying height sliders, we reveal the contributions of the potentially related physical models to the lubricant migration. We also reveal the contribution of the oscillating polar components of the disjoining pressure, which has not been modeled in the earlier studies. We further demonstrate the lubricant migration for various slider designs and flying conditions.

3.  3-dimensional partial wetting lubricant flow gorverning equations

   We adopt a 3-dimensional partial wetting lubricant flow governing equation, which is based on a continuum thin film lubrication theory [3] with a precursor film [4],  as given by equation (1) (see[5-6]). Here $h_L$ is the lubricant thickness, $t$ is time, $\mu_L$ is the lubricant viscosity, $p_L$ is the lubricant pressure, $\tau_L$ is the lubricant shear stress, $x$ is the coordinate in the slider's length direction and $y$ is the coordinate in its width direction.

$$\frac{\partial h_L}{\partial t} - \frac{1}{3\mu_L}\frac{\partial}{\partial x}\left(\frac{\partial p_L}{\partial x}h_L^3\right) + \frac{1}{2\mu_L}\frac{\partial}{\partial x}\left(\tau_{Lx}h_L^2\right)$$
$$-\frac{1}{3\mu_L}\frac{\partial}{\partial y}\left(\frac{\partial p_L}{\partial y}h_L^3\right) + \frac{1}{2\mu_L}\frac{\partial}{\partial y}\left(\tau_{Ly}h_L^2\right) = 0 \tag{1}$$

Considering the pressure and shear stress balance on the interface, the lubricant pressure and shear stress are given by equations (2)-(6) ( see [5-6]). We consider the air bearing pressure, the dispersive and polar components of disjoining pressure, the dispersive and polar components of Laplace pressure, and the air bearing shear stress and shear stress caused by the surface free energy gradient in our governing equations. The polar component of the disjoining pressure is modeled by a sinusoidal oscillation with an exponential decay envelope as proposed by Izumisawa et al [7].

In the governing equations below, $p_G$ is the air bearing pressure, $\Pi_{dis}$ and $\Pi_{pol}$ are the dispersive and polar components of the disjoining pressure, $\gamma_L$ is the surface free energy of the lubricant, $A$ is the Hamakar constant of the lubricant, $l_0$ is a correlation length for the polar endgroup, $S_0^p$ is the polar spreading coefficient for a bulk perflouro-polyether (PFPE) system, $\Delta\gamma_L^p$ is the surface energy amplitude, $h_m$ is the monolayer thickness of the lubricant, $\alpha$ is the phase shift parameter and $\tau_G$ is the air bearing shear stress.

$$p_L = p_G - \Pi_{dis} - \Pi_{pol} - \gamma_L\left(\frac{\partial^2 h_L}{\partial x^2} + \frac{\partial^2 h_L}{\partial y^2}\right) \tag{2}$$

$$\Pi_{dis} = -\frac{A}{6\pi h_L^3} \tag{3}$$

$$\Pi_{pol} = \frac{1}{l_0}\left\{S_0^P + \frac{\Delta\gamma_L^P}{h_m}C\sin\left(\frac{\pi h_L}{h_m} + \phi\right)\right\}\exp\left(-\frac{h_L}{l_0}\right) \tag{4}$$

$$C = \sqrt{\pi^2 l_0^2 + h_m^2}, \quad \phi = \alpha + \tan^{-1}\left(\frac{h_m}{\pi l_0}\right) \tag{5}$$

$$\tau_{Lx} = \tau_{Gx} + \frac{\partial \gamma_L}{\partial x}, \quad \tau_{Ly} = \tau_{Gy} + \frac{\partial \gamma_L}{\partial y} \tag{6}$$

The governing equation for the air bearing is the molecular gas lubrication (MGL) equation (7) [8], which is the so-called Fukui- Kaneko (F-K) Boltzman model. Here, $h_G$ is the local air bearing spacing, $\mu_G$ is the air viscosity and $Q$ is a flow factor. Considering the rarefaction effect, we used equation (8) for the air bearing shear stress calculation.

$$\frac{\partial (p_G h_G)}{\partial t} - \frac{1}{12\mu_G} \frac{\partial}{\partial x} \left( Q p_G h_G^3 \frac{\partial p_G}{\partial x} \right) + \frac{1}{2} u_x \frac{\partial}{\partial x} \left( p_G h_G \right)$$
$$- \frac{1}{12\mu_G} \frac{\partial}{\partial y} \left( Q p_G h_G^3 \frac{\partial p_G}{\partial y} \right) + \frac{1}{2} u_y \frac{\partial}{\partial y} \left( p_G h_G \right) = 0 \tag{7}$$

$$\tau_{Gx} = -\frac{h_G}{2} \frac{\partial p_G}{\partial x} w_p + \frac{\mu_G u_x}{h_G} w_c$$
$$\tau_{Gy} = -\frac{h_G}{2} \frac{\partial p_G}{\partial y} w_p + \frac{\mu_G u_y}{h_G} w_c \tag{8}$$

4. Numerical simulation method

The finite volume method is employed to discretize the lubricant flow governing equations. For spatial discretization we apply Patankar's power law method [9] and the Alternating Direction Implicit (ADI) method. In order to obtain faster simulation, we also apply an adaptive time stepping method. The air bearing pressure and shear stress are calculated by the program CMLAir [10], which is an air bearing solver developed at the Computer Mechanics Laboratory at the University of California, Berkeley. We assume that the air bearing pressure and shear stress are quasi static. .

5. CML 7nm slider at the inner radial position

5.1. Simulation condition for the CML 7nm slider inner radial position

Figure 1 shows a schematic of the simulation condition. This slider is called the CML

7nm slider, which is a pico size (1.2 x 1.0 mm) "negative-pressure" type slider. The disk rotational speed is 7,200 rpm, the radius of the slider flying track is 15.0 nm and the skew angle is 0.0 deg. The minimum flying height is 7.86 nm, pitch angle is 116.9 urad and roll angle is -1.80 urad. The initial lubricant thickness is taken as 2.0 nm on the highest (no-etch) air bearing surface. On the lower surfaces, the initial lubricant thickness is 0.001 nm. The lubricant viscosity coefficient, lubricant surface free energy and Hamakar constant are 0.144 Pas, 0.020 N/m and $-1.0 \times 10^{-21}$ J, respectively. Fig.2 (a) shows the rail geometry on the slider surface.


5.2. Simulation results for the CML 7nm slider inner radial position

Figure 2 shows the (a) slider geometry, (b) air bearing pressure distribution, (c) air bearing shear stress Poiseuille flow component distribution, (d) air bearing shear stress Couette flow component distribution, (e) total air bearing shear stress distribution, (f) air bearing shear stress Poiseuille flow component direction vectors, (g) air bearing shear stress Couette flow component direction vectors, (h) total air bearing shear stress direction vectors. The unit in all of the figures (b)-(e) is Pa.

The maximum value of the air bearing pressure is about 0.5 MPa. The maximum value of the air bearing shear stress is only about 0.002 MPa. Thus the maximum value of air bearing shear stress is less than 1 percent of the air bearing pressure. On the other hand, the maximum value of Poiseuille flow component is about 1200 Pa and the maximum value of the Couette flow component is about 1400 Pa. So, the Poiseuille flow component and the Couette flow component are of similar magnitude. But the distributions of those two components are quite different. For the Poiseuille flow component there are some relatively large magnitude areas near the edge of the rail, but at most of the slider surfaces the magnitude of the Poiseuille flow component is relatively small. By contrast, the magnitude

of the Couette flow component is relatively large over the large surfaces where the spacing is relatively small.

Furthermore, the directions of the Poiseuille flow component and the Couette flow component are very different. Because the direction of the Couette flow component corresponds to the direction of disk rotation, the vectors of the Couette flow component are pointing almost in the same direction. In the other hand, because the Poiseuille flow component is caused by the gradient of the air bearing pressure, the vectors of the Poiseuille flow component are very different from each other.

The vectors of the total air bearing shear stress on the relatively low flying height regions are pointing toward the trailing edge of the slider. But the vectors of the total air bearing shear stress on the relatively high flying height regions are very different from each other. Some of them are pointing toward the trailing edge of the slider, and some of them are pointing toward the leading edge of the slider. Consequently, there are some areas with zero shear stress which can be viewed as a stagnation point of the shear stress vectors. These areas are caused by the combination of the Poiseuille flow component and the Couette flow component of the air bearing shear stress.

Fig.3 shows the lubricant thickness evolution with time. The initial lubricant thickness on the top surface is 2.0nm (Fig.3 (a)) as mentioned above. After several tens of seconds of flying the lubricant migrates relatively quickly, and the lubricant thickness decreases on the top surface of the slider (Fig.3 (b), (c)). By contrast, the lubricant relatively slowly migrates on the deep recessed surface region (Fig.3 (c)-(f)). After several hundred seconds of slider flying the lubricant accumulates at specific regions on the deep recessed surface (Fig.3 (e), (f)).

We also investigated the correlation between the lubricant flow and the air bearing forces,

and we found the following: 1) The high air bearing shear stress regions (Fig.2 (d)) correspond to the relatively quick lubricant migration regions (Fig.3 (a)-(c)), while 2) the low air bearing shear stress regions (Fig.2 (d)) correspond to relatively slow migration regions (Fig.3(c)-(f)). 3) The accumulation regions (Fig.3 (f)) correspond to very small air bearing shear stress regions (Fig.2 (c) and (d)). We also found that 4) the lubricant migration direction primarily corresponds to air bearing shear stress direction.

6.   The effect of each parameter

  So far we have described the lubricant flow simulation results for the CML 7nm slider at the inner radius position. Next, we investigate the effect of each of the related parameters on the lubricant film thickness change for the CML 7nm slider at the inner radial position. Here, we investigate the effect of the precursor film thickness, lubricant viscosity coefficient, initial lubricant thickness, the lubricant surface free energy and the lubricant disjoining pressure.

6.1.   Effect of the precursor film thickness

  We first investigate the effect of the precursor film thickness. We employ the precursor film model in our partial wetting lubricant migration simulation to simplify the lubricant migration boundary condition. In order to reveal the contribution of the precursor film thickness on the lubricant film evolution we carried out simulations with different precursor film thicknesses b: b=0.01nm, b=0.001nm, and b=0.0001nm. All of the other parameters have the above mentioned values.

  Figures 4-6 show the simulation results for the three different precursor film thicknesses. Because the simulation results are very similar in all of the precursor film thicknesses we conclude that the precursor film thickness does not significantly affect the lubricant film

evolution. In other words, the precursor film thickness value b=0.001nm is thin enough for the lubricant flow system we focused on.

### 6.2.    Effect of the spatial discretization method

In the above we applied Patankar's power law method for the spatial discretization in our newly developed lubricant migration solver. In order to check the effect of the spatial discretization method on the lubricant evolution we carried out the lubricant flow simulations with some different spatial discretization methods. Here, we employ the upwind method, the hybrid method and the power law methods of spatial discretization. All of the parameters keep the above mentioned values.

Figures 7-9 show the simulation results using the different spatial discretization methods. All of these simulation results are very similar and the computational times are almost the same, about 2 minutes (grid size: 145 x 145, simulation time: 400 sec) for all spatial discretization methods. Therefore, henceforth we employ the power law method, which has been recommended by Patankar in our lubricant migration solver.

### 6.3.    Effect of the lubricant viscosity

The lubricant viscosity coefficient varies substantially with temperature. Some lubricant viscosity coefficients increase by a factor of 100 at low enough temperatures. So, the lubricant viscosity coefficient is one of the important parameters in the lubricant migration. In order to reveal the effect of the lubricant viscosity coefficient on the lubricant evolution we carried out lubricant flow simulations with three different lubricant viscosity coefficients.:1.44 Pas, 0.144 Pas and 0.0144 Pas. All other parameters are the same as the above mentioned values.

Figures 10-12 show the simulation results with the three lubricant viscosity coefficients. Because the simulation results are very different for the different lubricant viscosity

coefficients, the importance of the lubricant viscosity coefficient to the lubricant migration evolution is considered quite significant. With a decrease in the viscosity coefficient, the mobility of lubricant gets higher. With an increase in the viscosity coefficient, the mobility of lubricant gets lower. The simulation results for the viscosity coefficient of 0.144 Pas at 10 sec corresponds to that of viscosity coefficient 1.44 Pas at 100 sec. The simulation results for the viscosity coefficient of 0.0144 Pas at 10 sec corresponds to that of viscosity coefficient 0.144 Pas at 100 sec. So, if the viscosity coefficient gets ten times it takes ten times longer to achieve the same result. If the viscosity coefficient gets ten times smaller it takes only one tenth of the time to achieve the same result. This tendency corresponds to equation (1) in which the inverse of the viscosity coefficient is equivalent to the time scaling.

6.4.    Effect of the initial lubricant film thickness

 In order to reveal the effect of the initial lubricant film thickness on the lubricant migration, we carried out the lubricant flow simulation with some different initial lubricant film thicknesses. Here, we employ 1nm, 2nm, and 4nm for the initial lubricant film thicknesss. All of the other are the same as above mentioned values.

 Figures 13-15 show the simulation results for each initial lubricant film thickness. Though the initial lubricant film thickness affects the lubricant profile evolution, the lubricant flow patterns are similar for each initial lubricant film thickness. If the initial lubricant film thickness is larger, the migration speed is faster. Those tendencies can be explained by examining equation (1) in which the flow rate is proportional to the second power or cube of the lubricant film thickness h.

6.5.    Effect of lubricant surface free energy

In order to reveal the effect of the lubricant surface free energy on the lubricant profile evolution, we carried out lubricant flow simulations with some different lubricant surface free energies; 10mN/m, 20mN/m and 30mN/m. All of the other parameters have the above mentioned values.

Figures 16-18 show the simulation results for the three different lubricant surface free energies. As seen there the lubricant evolution is quite similar in all cases. So, the lubricant surface free energy has a minor effect on the lubricant migration. This is caused by the small contribution of the Laplace pressure to the lubricant evolution, as we describe below.

## 6.6.    Effect of the lubricant disjoining pressure (Hamakar constant)

In order to reveal the effect of the lubricant disjoining pressure on the lubricant migration, we carried out lubricant flow simulations for three different lubricant Hamakar constants; -1.0E-20 J, -1.0E-21 J and -1.0E-22 J. All of the other parameters are the same as the above mentioned values.

Figures 19-21 show the simulation results for the three lubricant Hamakar constants. The lubricant evolution profiles look similar for all three values. But, the diffusion of the lubricant film thickness is different for the different Hamakar constants. If the Hamakar constant is large, the lubricant film is easily diffused. This tendency can be explained by examining the transformed governing equation in which the lubricant disjoining pressure term appears as a diffusion term.

So far, we have investigated the effects of several related parameters and models on the lubricant evolution. As a result of this investigation, we revealed the following.

1)  A precursor film thickness of 0.001nm is sufficient to set the advancing boundary

condition.

2) The lubricant viscosity coefficient largely affects the migration evolution as a time scaling factor.

3) Though the initial lubricant thickness largely affects the lubricant evolution, the flow pattern does not change much with thickness.

4) The lubricant surface energy hardly affects the lubricant profile evolution.

5) The disjoining pressure largely affects the lubricant distribution as a diffusion factor.


7.  Contribution of related physical models

  The lubricant migration on a slider surface is affected by many physical models. It is important to reveal which physical models are major factors and which are minor ones. Such results will provide useful knowledge for understanding these complex phenomena. We investigated the contribution of the related physical models in the governing equations. In order to quantify the individual contributions, we removed various terms from the simulation equation sequentially. All of the parameter values are the same as mentioned above.

  Figures 22-26 show the simulation results out one physical model removed from the equation. From the simulation results, we find the following.


1) Air bearing pressure

  Because the lubricant evolution without air bearing pressure is very similar to that with it, we can conclude that the contribution of air bearing pressure to the lubricant migration is very small.

2) Air bearing shear stress

  The lubricant evolution without air bearing shear stress is very different from that with it

retained. Without the air bearing shear stress the lubricant thickness hardly changes. So the air bearing shear stress has a dominant effect on the lubricant thickness change, and it is a driving factor of lubricant migration.

3) Lubricant disjoining pressure

Though the lubricant evolution without disjoining pressure is similar to that with it included, the disjoining pressure has a large effect on the lubricant evolution. Because the Hamakar constant is quite small in this simulation, large difference between the lubricant evolution is not seen when it is removed from the equation.

4) Laplace pressure

Because the lubricant evolution without the Laplace pressure is very similar to that with it included, the contribution of Laplace pressure to the lubricant migration is small. Unlike the case for the disk surface, the slider surface has concavity and convexity whose height is in micrometers. The Laplace pressure is a function of curvature of the lubricant interface. So, the contribution of Laplace pressure on the slider surface is larger than that on the disk surface. But, the Laplace pressure on the slider surface still does not largely affect the lubricant evolution.

From the above results we can conclude the following. The air bearing shear stress has a dominant effect on the lubricant evolution, and the disjoining pressure also has a certain effect on the lubricant evolution as a diffusion factor. By contrast, the air bearing pressure and the Laplace pressure have minor effects on the lubricant evolution.

8. The effect of the slider's flying condition

Heretofore we carried out lubricant migration simulation for the CML 7nm slider with zero skew angle, and the contributions of related physical models were revealed. In order to

investigate the effect of the slider's flying condition, we performed lubricant flow simulations with several skew angles and radii. All of the other parameters were the same as above mentioned values.

8.1.   Simulation results for the CML 7nm slider at the center radial position

Figure 27 shows the slider geometry, air bearing pressure and shear stress for the CML 7nm slider at the inner radial position. Figure 27(a) shows the slider geometry, (b) the air bearing pressure distribution, (c) the air bearing shear stress Poiseuille flow component distribution, (d) the air bearing shear stress Couette flow component distribution, (e) the total air bearing shear stress distribution, (f) the air bearing shear stress Poiseuille flow component direction vectors, (g) the air bearing shear stress Couette flow component direction vectors, and (h) the total air bearing shear stress direction vectors. The units in all of the figures (b)-(e) are Pa.

Figure 28 shows the lubricant thickness evolution with time under the CML 7nm slider at the center radial position and inner radial position. The lubricant migrations in both positions share similar features, which are discussed for the inner position. (1) After several tens of seconds of the slider flying the lubricant migrates relatively quickly and the lubricant thickness relatively quickly decreases on the top surface of the slider. (2) By contrast, the lubricant relatively slowly migrates on the deep recessed surface region. (3) After about several hundred seconds of slider flying, the lubricant accumulates at specific regions on the deep recessed surface. Those characteristics are observed at both the inner and center radial positions, but the flow patterns are different at the two positions. Two differences are observed. The first difference is in the lubricant flow direction. The lubricant mainly migrates toward the trailing edge at the radial inner position. But, the

15

lubricant mainly migrates towards a slightly inner direction in the center radial position. Because the skew angle at the center radial position is 0.0 deg and the skew angle in the inner radial position is 9.1 deg, this difference is evidently caused by the skew angle. The second difference is the speed of lubricant migration. The lubricant migration speed in the inner radial position is faster than at the inner position. Because the disk velocity at the inner radial position is faster than that at the inner radial position, the Couette flow component of the air bearing shear stress at the center radial position is larger than at the inner position. This difference causes the faster migration speed at the inner radial position.

8.2.   Simulation results for the CML 7nm slider at the outer radial position

 Figure 29 shows the slider geometry, air bearing pressure and shear stress under the CML 7nm slider at the outer radial position. Figure 29 (a) shows the slider geometry, (b) the air bearing pressure distribution, (c) the air bearing shear stress Poiseuille flow component distribution, (d) the air bearing shear stress Couette flow component distribution, (e) the total air bearing shear stress distribution, (f) the air bearing shear stress Poiseuille flow component direction vectors, (g) air bearing shear stress Couette flow component direction vectors, and (h) the total air bearing shear stress direction vectors. The units in Figures (b)-(e) are Pa.

 Figure 30 shows the lubricant thickness evolution with time under the CML 7nm slider at the outer radial position and center radial position. The lubricant migrations in both positions share similar features, which are described for the inner radial position. (1) After several tens of seconds of the slider flying, the lubricant migrates relatively quickly and the lubricant thickness relatively quickly decreases on the top surface of the slider. (2) By

contrast, the lubricant relatively slowly migrates on the deep recessed surface region. (3) After several hundred seconds of slider flying, the lubricant accumulates at specific regions on the deep recessed surface. Those characteristics are observed at both the center and outer radial positions, but the flow patterns are different for these two positions. Two differences in the flow pattern are observed. The first difference is in the lubricant flow direction. The second difference is the speed of lubricant migration. Those differences are caused by the change in the skew angle and disk speed as we mentioned for the inner position case.

Further simulations were carried out for the CML 7nm slider at three radial positions and we observed the changes in lubricant flow pattern.

9. The effect of the air bearing surface design

In order to investigate the effect of the air bearing surface design, we performed lubricant flow simulations with several different air bearing surface designs. All of the parameters except air bearing surface design and flying conditions were kept the same as the above mentioned values.

9.1. Simulation results for the CML femto slider

Figure 31 shows the slider geometry, air bearing pressure and shear stress for the CML femto slider. Figure 31(a) shows the slider geometry, (b) the air bearing pressure distribution, (c) the air bearing shear stress Poiseuille flow component distribution, (d) the air bearing shear stress Couette flow component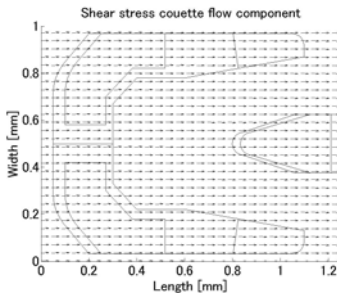 distribution, (e) the total air bearing shear stress distribution, (f) the air bearing shear stress Poiseuille flow component direction vectors, (g) air bearing shear stress Couette flow component direction vectors, and (h) the total air bearing shear stress direction vectors. The units in Figures (b)-(e) are Pa.

Figure 32 shows the lubricant thickness evolution with time for the CML femto slider. The lubricant migrations under the CML femto slider have the same three features that were observed for the CML 7nm slider. (1) Relatively faster lubricant migration speeds on the ABS (no-etch) surface, (2) relatively slow lubricant migration speeds on the deep recessed region and (3) the accumulation of lubricant at specific regions. But, the flow patterns are largely different between CML 7nm slider and CML femto slider.

9.2.    Simulation results for the Data Storage Institute (DSI) femto slider

Figure 33 shows the slider geometry, air bearing pressure and shear stress for the DSI femto slider. Figure 33(a) shows the slider geometry, (b) the air bearing pressure distribution, (c) the air bearing shear stress Poiseuille flow component distribution, (d) the air bearing shear stress Couette flow component distribution, (e) the total air bearing shear stress distribution, (f) the air bearing shear stress Poiseuille flow component direction vectors, (g) the air bearing shear stress Couette flow component direction vectors, and (h) the total air bearing shear stress direction vectors. The units in Figures (b)-(e) are Pa.

Figure 34 shows the lubricant thickness evolution with time under the DSI femto slider. The lubricant migrations have the same three features observed for the CML 7nm slider and CML femto slider. But, the flow patterns are largely different between CML sliders and DSI femto slider.

10.  The effect of the oscillatory polar component of the lubricant disjoining pressure

In order to investigate the effect of the oscillatory polar component of lubricant disjoining pressure we carried out the lubricant migration simulation with this effect included. We

model the oscillatory polar component of disjoining pressure using the sinusoidal oscillation model with exponential decay, which has been proposed by Izumisawa et al [7]. The parameters used by Izumisawa et al. were $l_0 = 1.0$ nm, $S_0^p = -1.4$ mN/m, $\Delta\gamma_L^p = 5.3 \times 10$ mN/m, $h_m = 1.2$ nm, $\alpha = -0.95$. These parameters are also used in this simulation. The Hamakar constant $A = -4.7 \times 10^{-20}$ J is also used. All of the parameters except the disjoining pressure are the same as for the CML 7nm slider at the inner radial position.

Figure 35 shows the lubricant thickness evolution with the oscillatory polar component of the lubricant disjoining pressure included. We see that the evolution is quite different from that when it is not included. In particular, when including the oscillatory polar component of disjoining pressure a lot of small lubricant droplets appear on the slider surface. This emergence of multiple droplets could be caused by the existence of discrete stable lubricant thicknesses due to the oscillatory polar component of the disjoining pressure.

11. Summary

Based on a continuum thin film lubrication theory with inter-molecular forces and a precursor film model we developed a simulator for predicting the lubricant migration on slider surfaces in hard disk drives. Using the newly developed solver we investigated the detailed lubricant migration behavior on a modern negative pressure type slider surface. We found distinct lubricant migration speeds, mainly depending on the etch depth of the slider surfaces and the accumulation of lubricant at specific regions. We found that the lubricant migration behavior largely correlates with the magnitude and direction of the air bearing shear stress. Moreover we revealed the contributions of the various physical models to the lubricant migration. We found that the air bearing shear stress has a dominant effect on the lubricant profile evolution and the disjoining pressure also affects

the lubricant evolution through diffusion. By contrast, the air bearing pressure and the Laplace pressure have minor effects on the lubricant thickness evolution. We also studied the contribution of the oscillatory polar component of the disjoining pressure, and we found that it causes multiple small lubricant droplets to emerge on the slider surface. We further demonstrated the lubricant migration on various different slider designs and flying conditions. We found that the slider design and flying condition largely affect the lubricant migration pattern.

References

[1] L. Wu, "Modeling and Simulation of the Interaction between 3-D Lubricant Droplets on the Slider Surface and Air Flow within the Head/Disk Interface of Disk Drives", Proc. IEEE International Magnetics Conference, San Diego, pp. 87, May, 2006

[2] B. Zhang and A. Nakajima, "Hydrodynamic Lubrication of Slider Air Bearings with Pumping Effect", Proc. Micromechatronics for Information and Precision Equipment, Santa Clara, June, 2006

[3] Oron, A., Davis, S. H., Bankoff, S. G., 1997, "Long-scale evolution of thin liquid films", Reviews of Modern Physics, Vol. 69, No. 3, 931-980.

[4] P.G. de Gennes, "Wetting: statics and dynamics", Rev. Mod. Phys., vol. 57, pp. 827-863, 1985

[5] K. Yorino, N. Konishi, K. Yamane, H. Matsuoka and S. Fukui, Proc. of JAST Tribology Conference, pp 343-344, 2004 (in Japanese)

[6] H. Kubotera and D.B. Bogy, "Numerical Simulation of Molecularly Thin Lubricant Film Flow", Proc. Micromechatronics for Information and Precision Equipment, Santa Clara, Santa Clara, June 2006.

[7] S. Izumisawa and Myung S. Jhon, "Stability analysis and molecular simulation of

nanoscale lubricant films with chain-end functional groups", Journal of Applied Physics, vol. 91, No. 10, pp 7583-7585, 2002.

[8] S. Fukui and R. Kaneko, "Molecular Gas Film Lubrication", Handbook of Micro/Nanotribology, CRC Press, pp. 559-603, 1995

[9] Patankar, S. V., 1980, Numerical Heat Transfer and Fluid Flow, McGraw-Hill, New York.

[10] Lu, S., 1997, "Numerical Simulation of Slider Air Bearings", Doctoral Dissertation, University of California at Berkeley.

CML slider (Pico)
flying height: 7.86 nm (min)
Pitch angle: 116.9 $\mu rad$
Roll angle: -1.80 $\mu rad$

Initial lubricant
thickness: 2.0nm

Disk rotation

Disk rotation: 7,200 rpm
Radius position: 15.0 mm
Skew angle: 0.0 deg
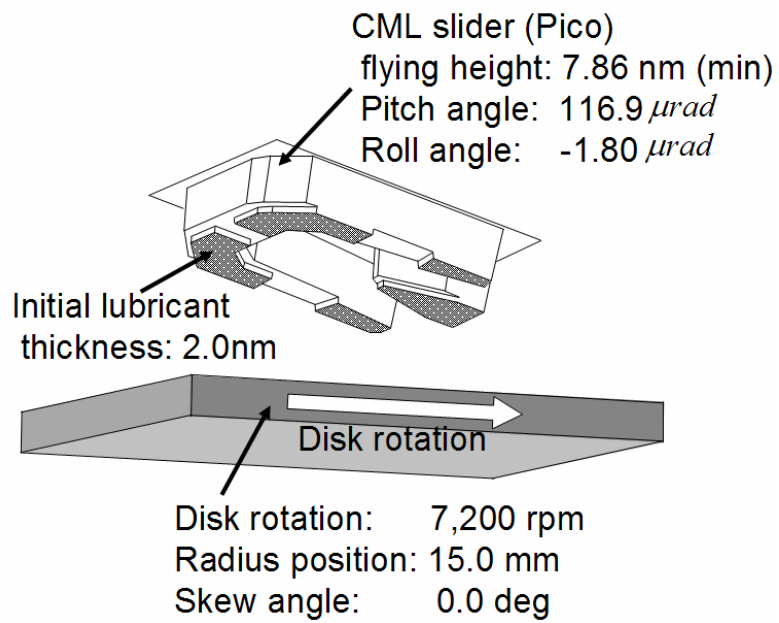
Figure 1 Schematic of simulation condition.
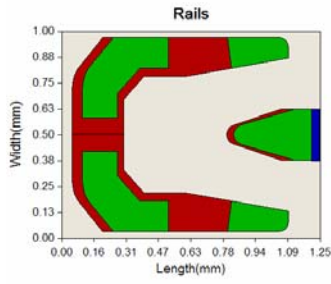
(a) slider geometry          (b) air bearing pressure
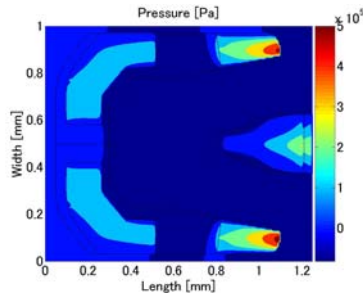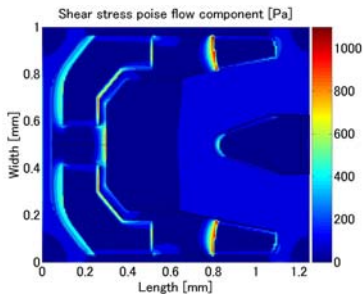


(c) air bearing shear stress      (d) air bearing shear stress      (e) total air bearing
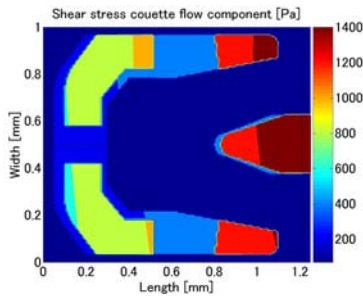
Poiseuille flow component        Couette flow component            shear stress
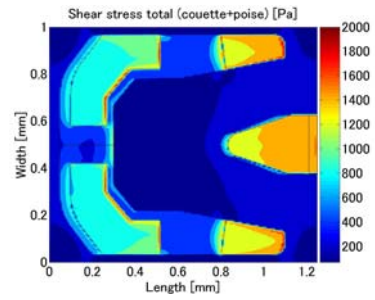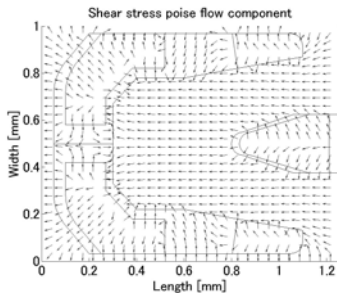


(f) air bearing shear stress      (g) air bearing shear stress      (h) total air bearing

Poiseuille flow component        Couette flow component            shear stress direction
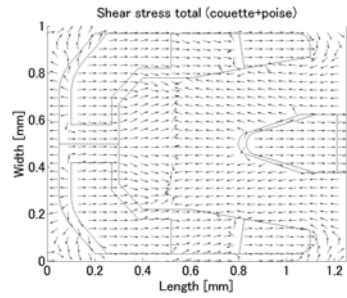
direction vectors                direction vectors                vectors

Figure.2 CML pico 7nm slider inner radial position, slider geometry and air bearing pressure and shear stress

(a) t=0.0 [s]  (b) t=10.0 [s]  (c) t=30.0 [s]



(d) t=100.0 [s]  (e) t=200.0 [s]  (f) t=300.0 [s]
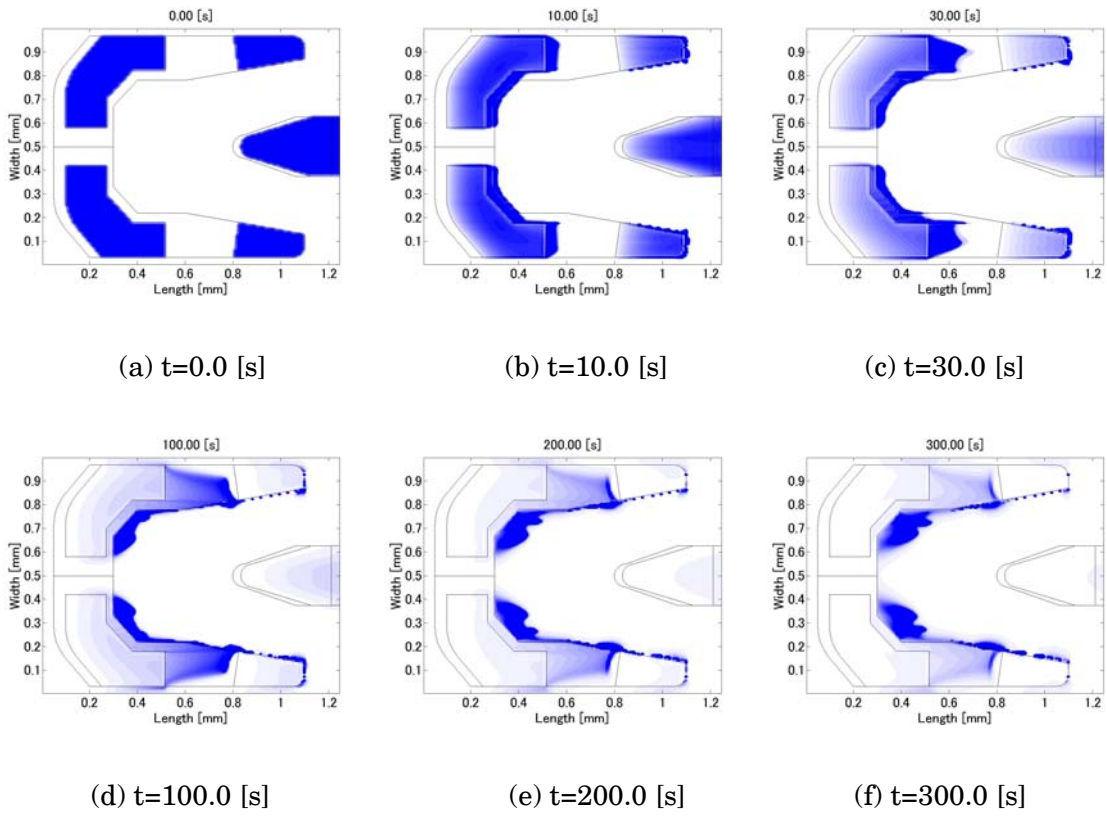
Figure.3 Simulation results under CML pico 7nm slider inner radial position
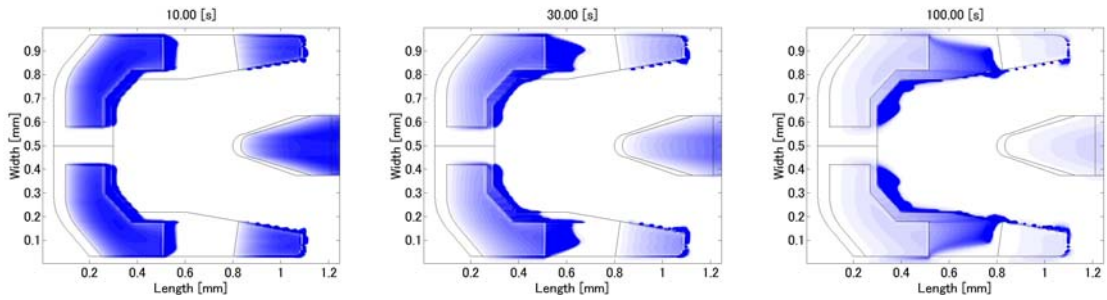


Fig.4 Simulation results under CML 7nm slider inner radial position with b=0.01nm
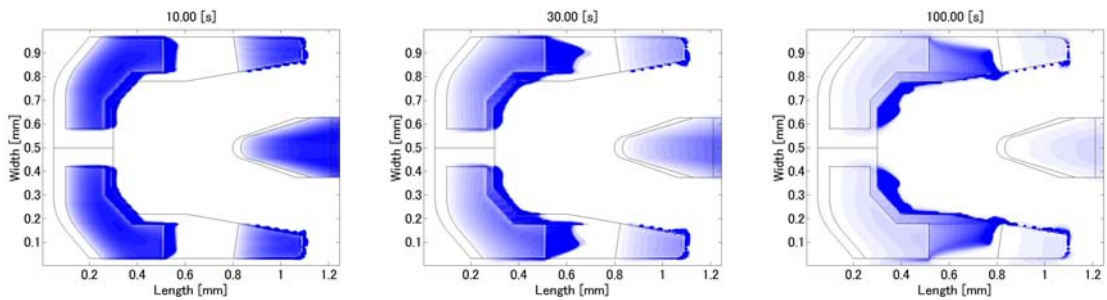
Fig.5 Simulation results under CML 7nm slider inner radial position with b=0.001nm
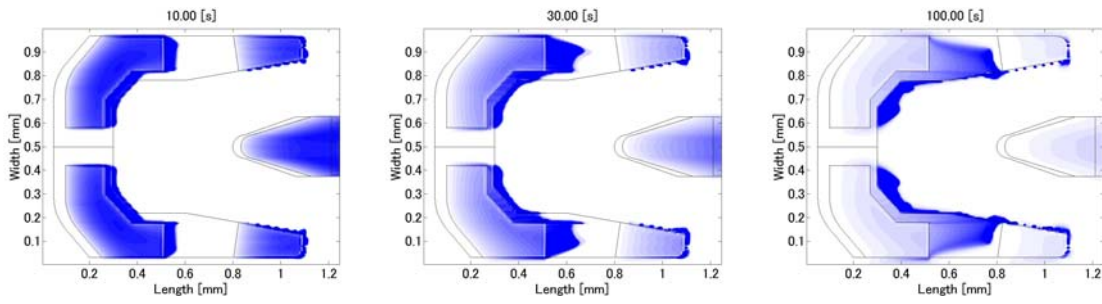


Fig.6 Simulation results under CML 7nm slider inner radial position with b=0.0001nm
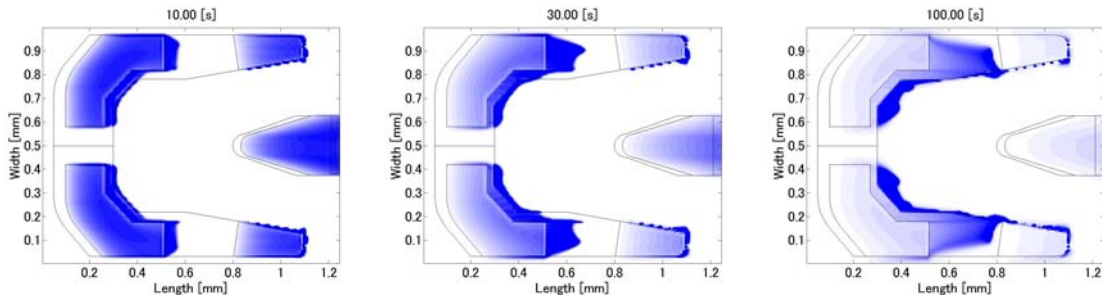


Fig.7 Simulation results under CML 7nm slider inner radial position with upwind method
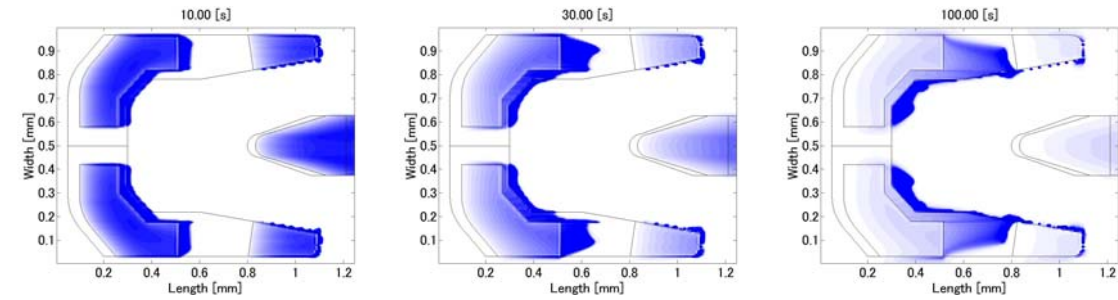


Fig.8 Simulation results under CML 7nm slider inner radial position with hybrid method
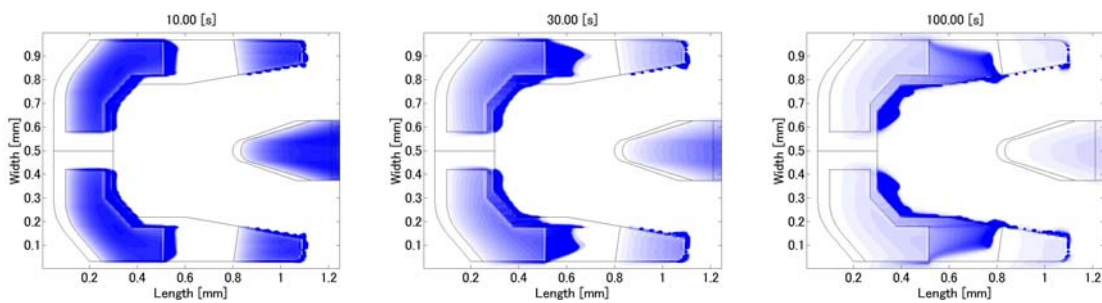
Fig.9 Simulation results under CML 7nm slider inner radial position with power method
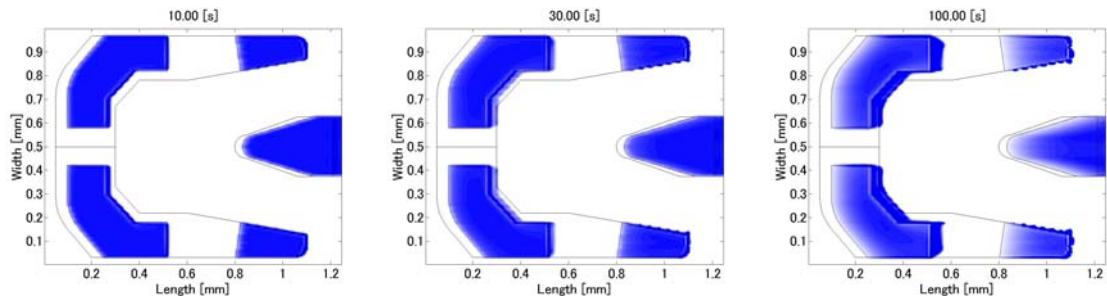


Fig.10 Simulation results under CML 7nm slider inner radial position with lubricant

viscosity coefficient 1.44 Pas
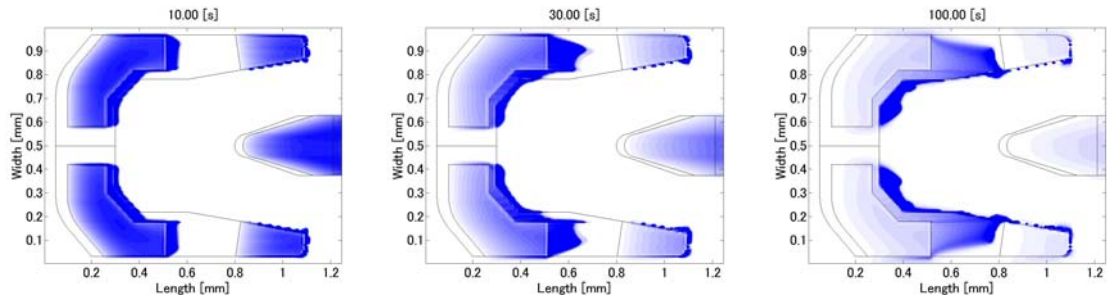


Fig.11 Simulation results under CML 7nm slider inner radial position with lubricant

viscosity coefficient 0.144 Pas
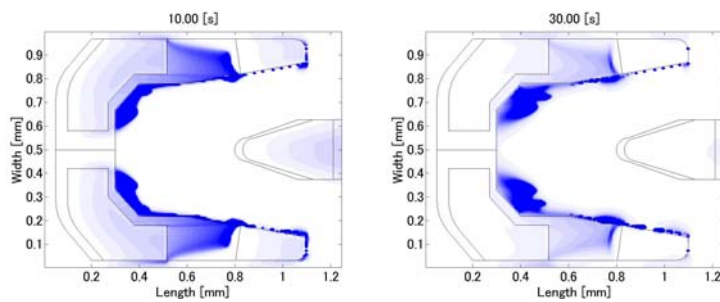


Fig.12 Simulation results under CML 7nm slider inner radial position with lubricant

viscosity coefficient 0.0144 Pas
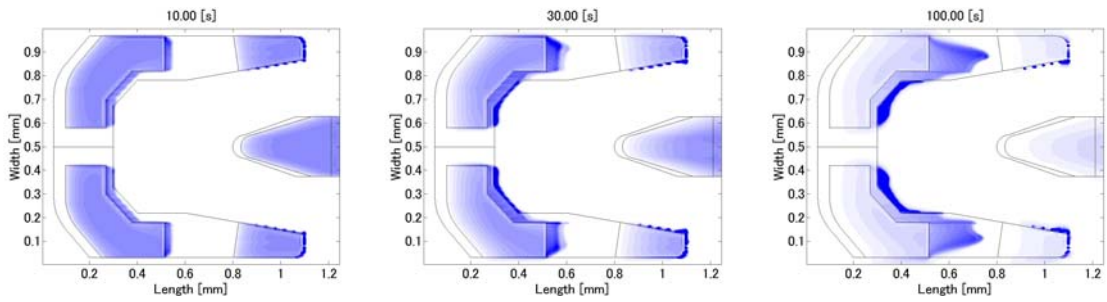
Fig.13 Simulation results under CML 7nm slider inner radial position with initial

lubricant thickness 1nm
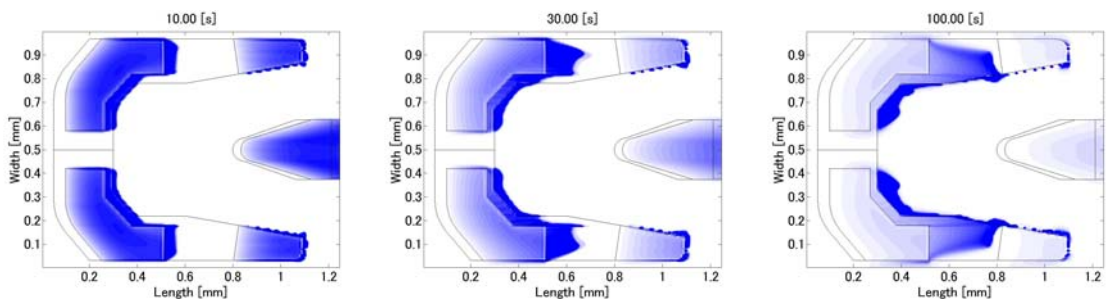


Fig.14 Simulation results under CML 7nm slider inner radial position with initial

lubricant thickness 2nm
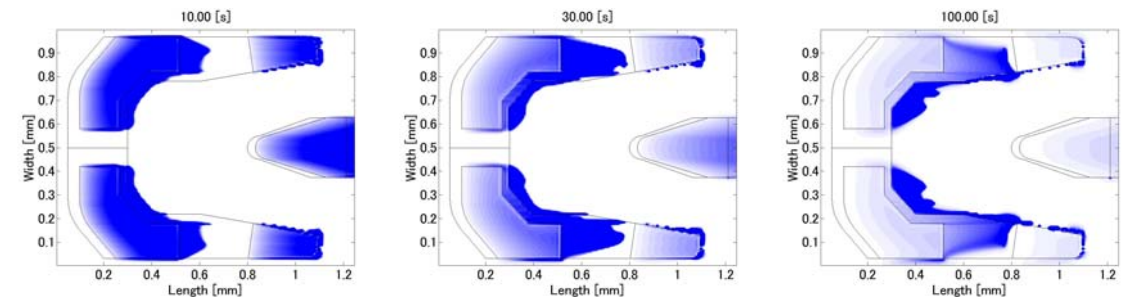


Fig.15 Simulation results under CML 7nm slider inner radial position with initial

lubricant thickness 4nm
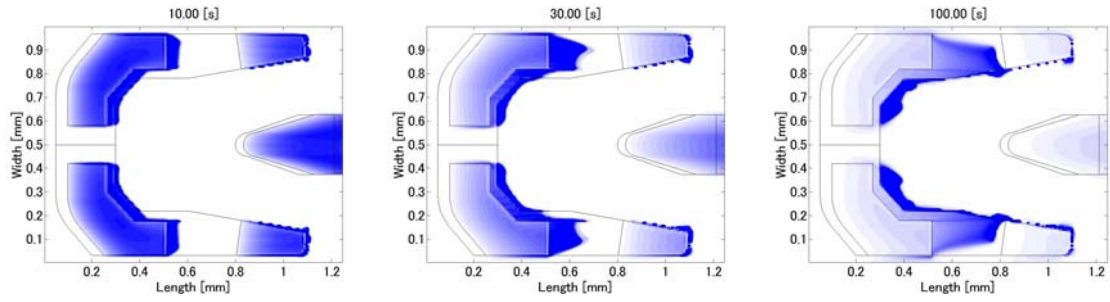
Fig.16 Simulation results under CML 7nm slider inner radial position with lubricant

surface free energy 10mN/m
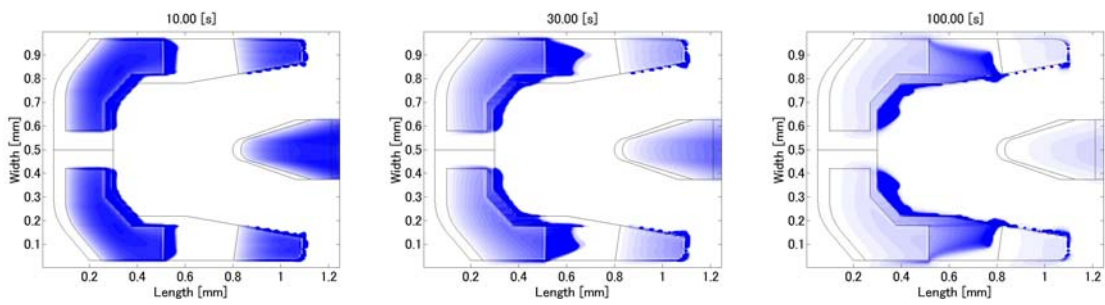


Fig.17 Simulation results under CML 7nm slider inner radial position with lubricant

surface free energy 20mN/m
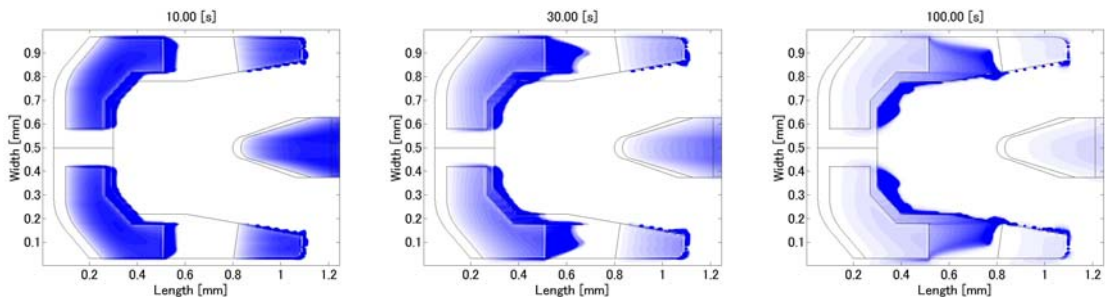


Fig.18 Simulation results under CML 7nm slider inner radial position with lubricant

surface free energy 30mN/m
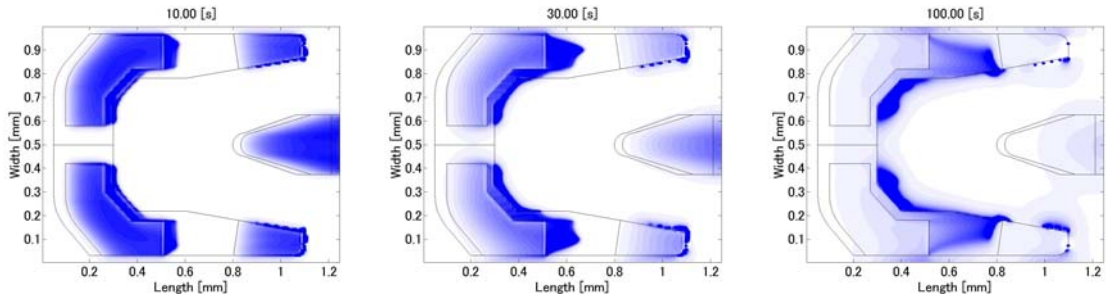
Fig.19 Simulation results under CML 7nm slider inner radial position with Ha= -1.0e-20J
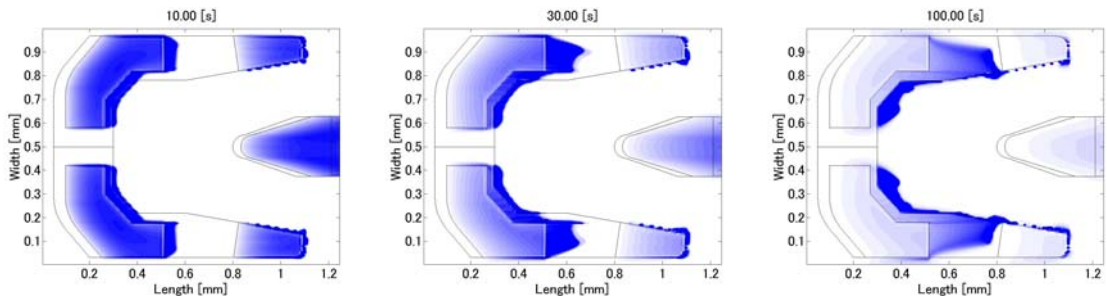


Fig.20 Simulation results under CML 7nm slider inner radial position with Ha= -1.0e-21J
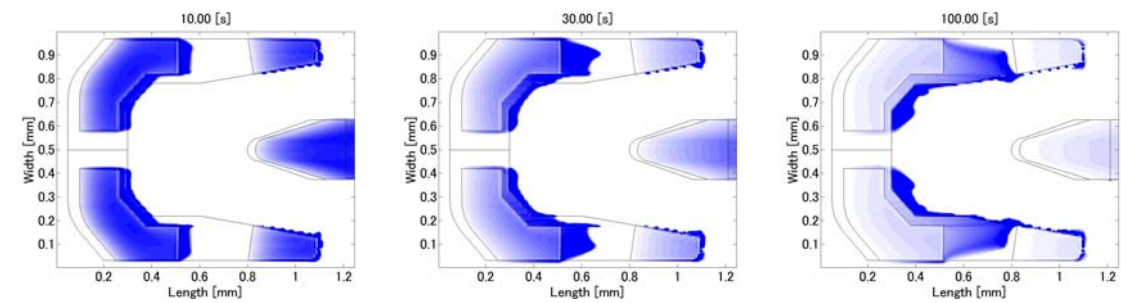


Fig.21 Simulation results under CML 7nm slider inner radial position with Ha= -1.0e-22J
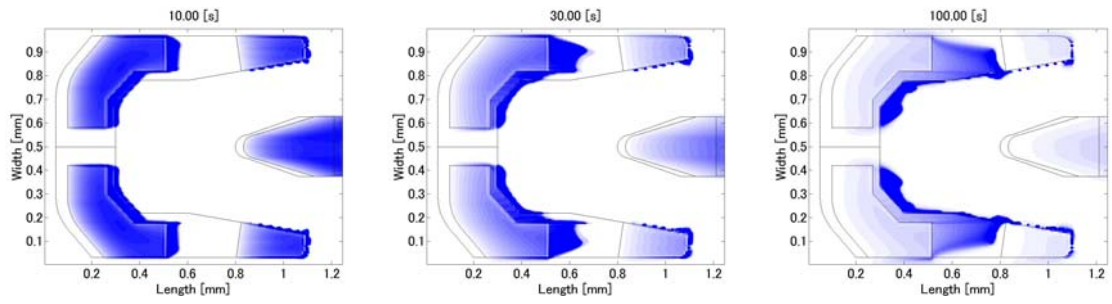
Fig.22 Simulation results under CML 7nm slider inner radial position with all physical

models
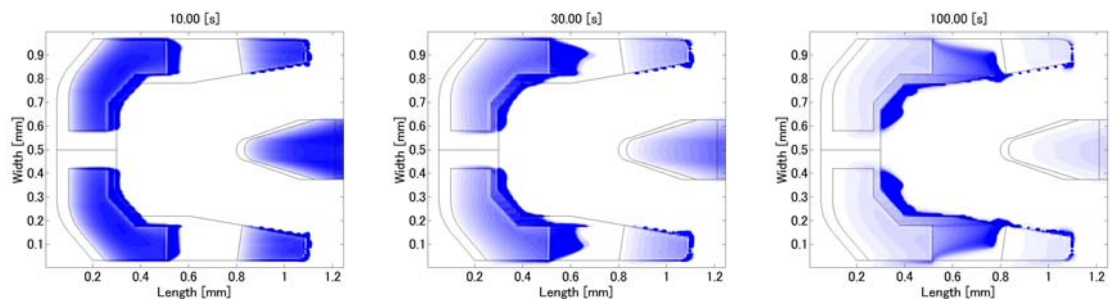


Fig.23 Simulation results under CML 7nm slider inner radial position

without air bearing pressure
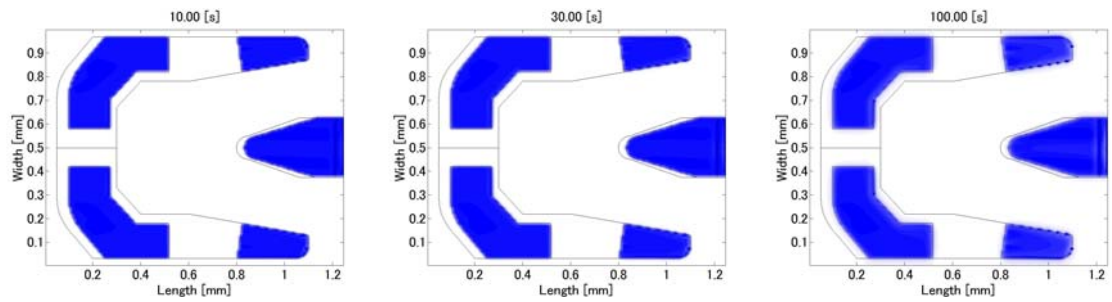


Fig.24 Simulation results under CML 7nm slider inner radial position

without air bearing shear stress
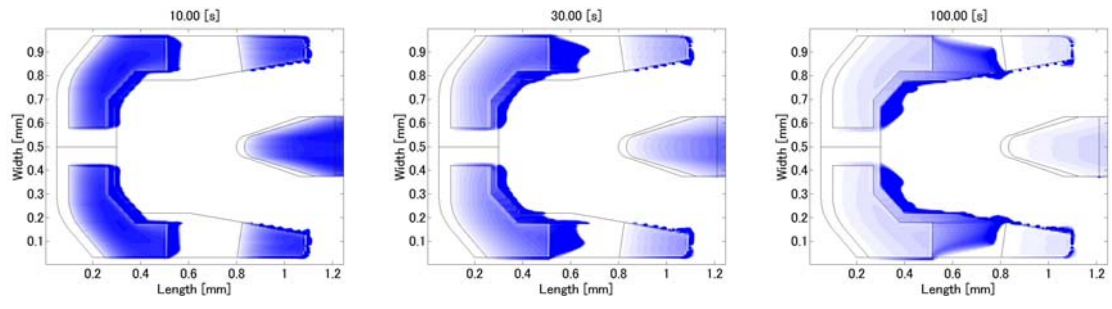
Fig.25 Simulation results under CML 7nm slider inner radial position

without disjoining pressure
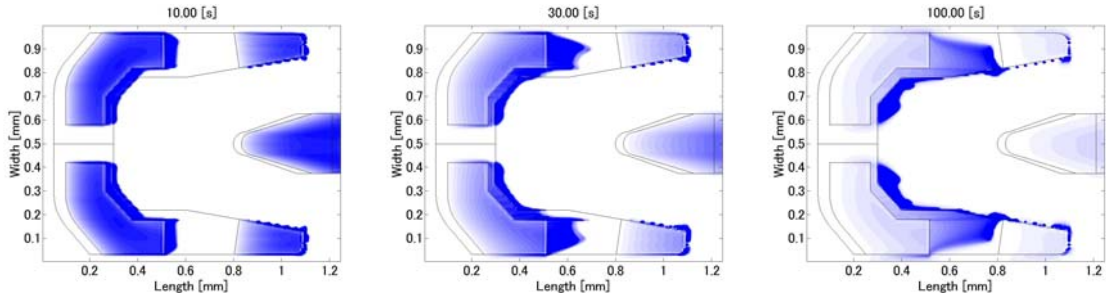


Fig.26 Simulation results under CML 7nm slider inner radial position

without Laplace pressure
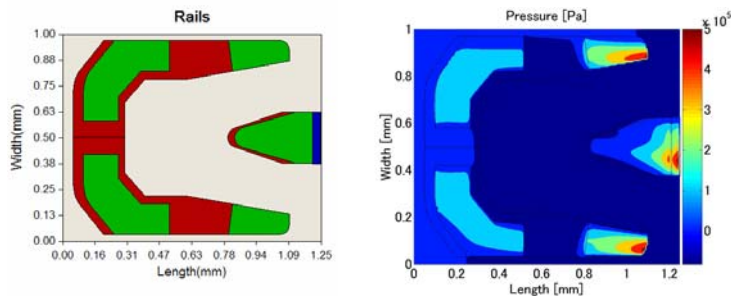


(a) slider geometry          (b) air bearing pressure
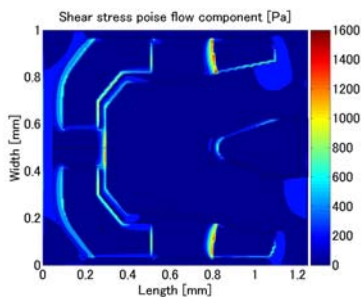


(c) air bearing shear stress          (d) air bearing shear stress          (e) total air bearing
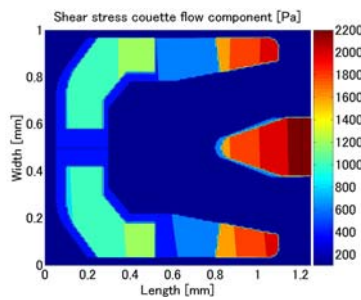
Poiseuille flow component          Couette flow component          shear stress
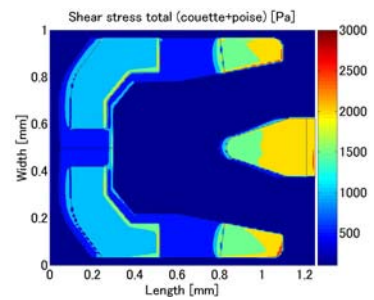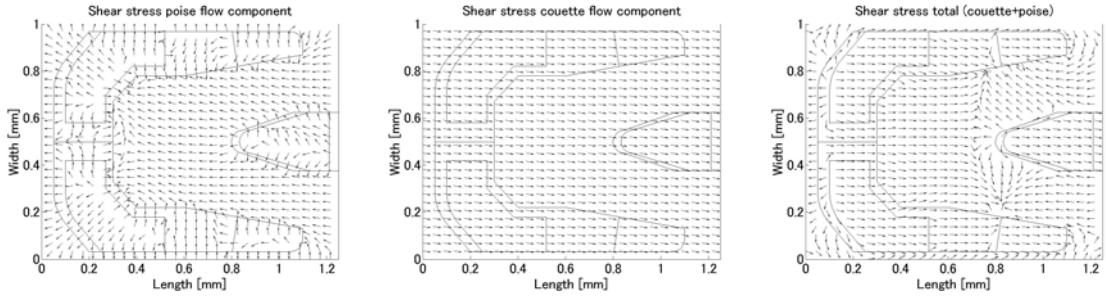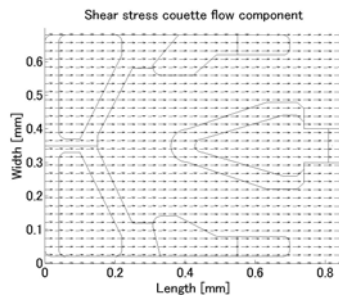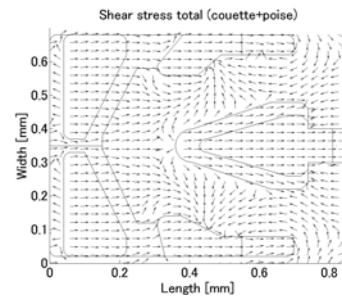
(f) air bearing shear stress Poiseuille flow component direction vectors

(g) air bearing shear stress Couette flow component direction vectors

(h) total air bearing shear stress direction vectors

Figure.27 CML pico 7nm slider center radial position, slider geometry and air bearing pressure and shear stress
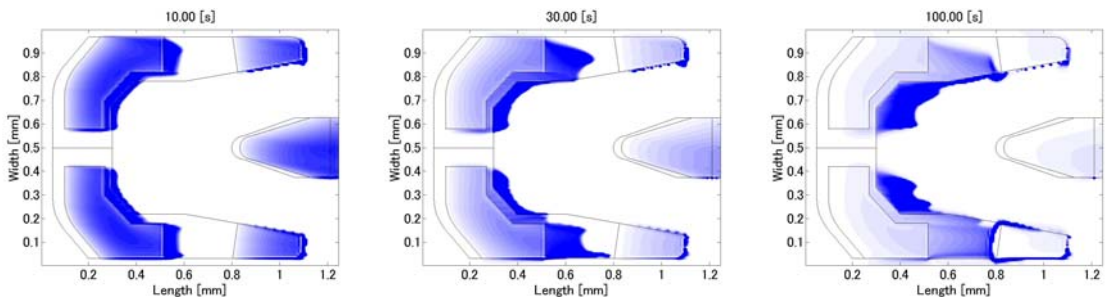


(a) Center, t=10.0 [s]

(b) Center, t=30.0 [s]

(c) Center, t=100.0 [s]
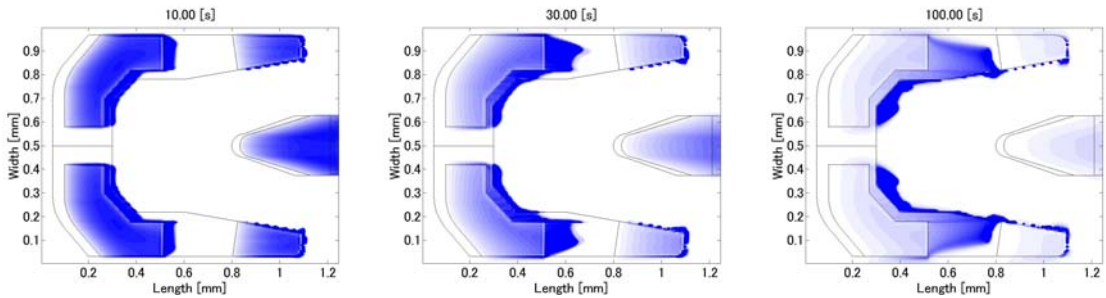
(d) Inner, t=10.0 [s]

(e) Inner, t=30.0 [s]

(f) Inner, t=100.0 [s]

Fig.28 Simulation results under CML 7nm slider center radial position (a)-(c).

Simulation results at inner radial position are showed as a reference (d)-(f).
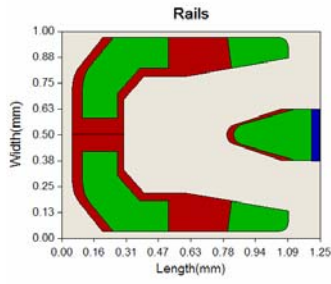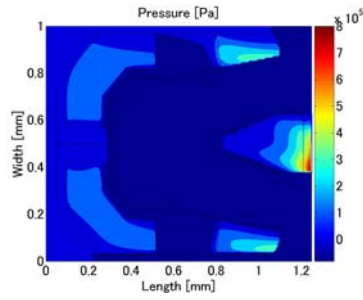
(a) slider geometry       (b) air bearing pressure
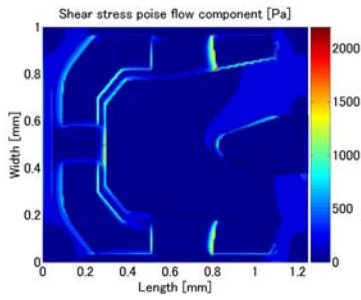


(c) air bearing shear stress

Poiseuille flow component
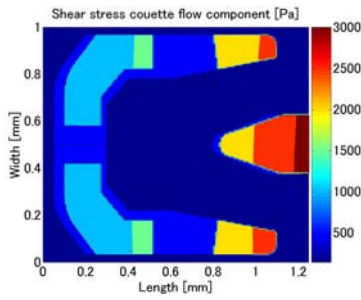
(d) air bearing shear stress

Couette flow component
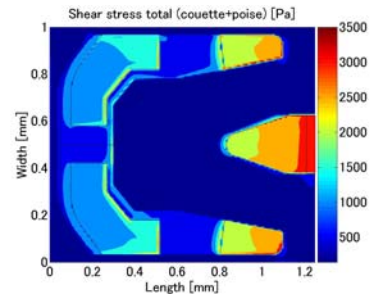
(e) total air bearing
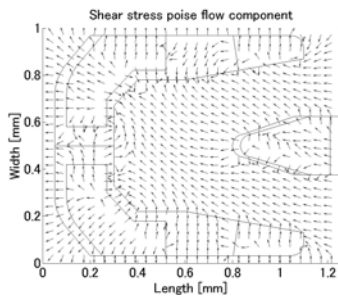
shear stress



(f) air bearing shear stress

Poiseuille flow component
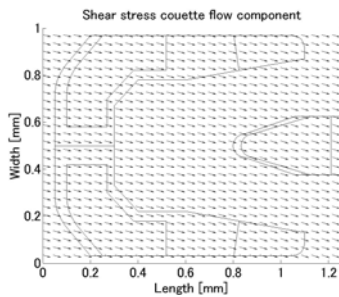
direction vectors
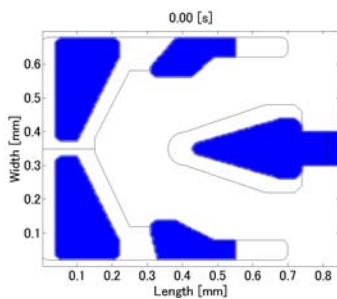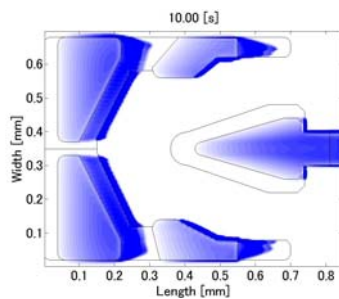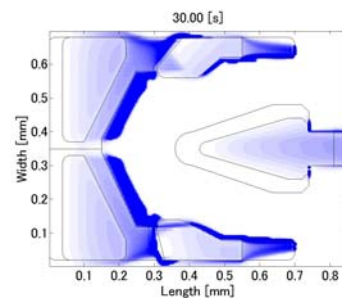
(g) air bearing shear stress

Couette flow component
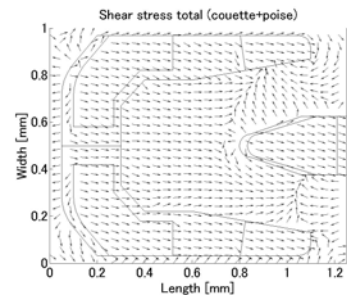
direction vectors

(h) total air bearing

shear stress direction

vectors

Figure.29 CML pico 7nm slider outer radial position, slider geometry and air bearing

pressure and shear stress
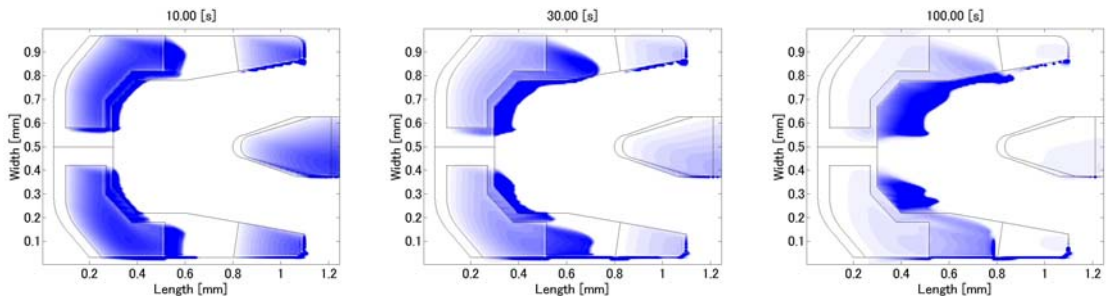
(a) OD, t=10.0 [s]　　　　(b) OD, t=30.0 [s]　　　　(c) OD, t=100.0 [s]
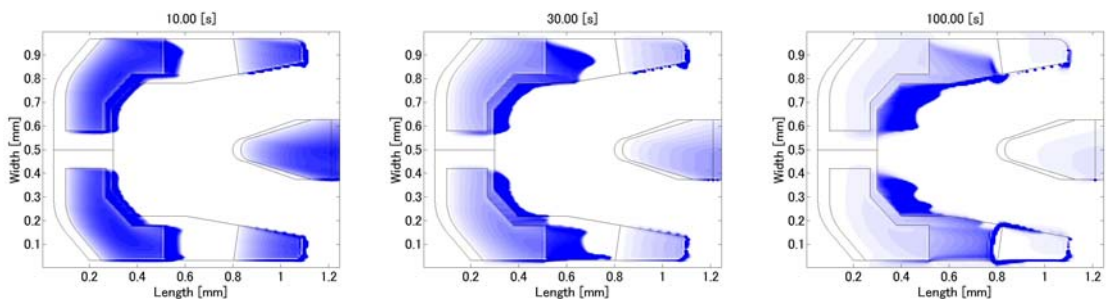
(d) MD, t=10.0 [s]　　　　(e) MD, t=30.0 [s]　　　　(f) MD, t=100.0 [s]

Fig.30 Simulation results under CML 7nm slider outer radial position (a)-(c).

Simulation results at center radial position are showed as a reference (d)-(f).
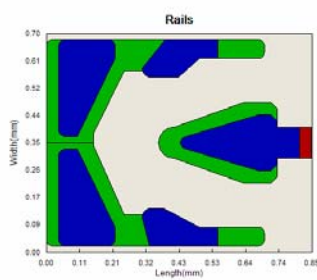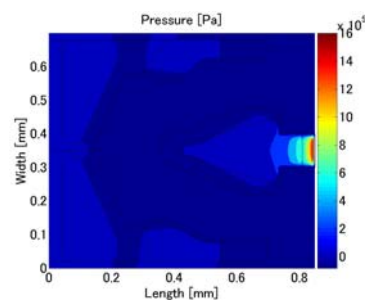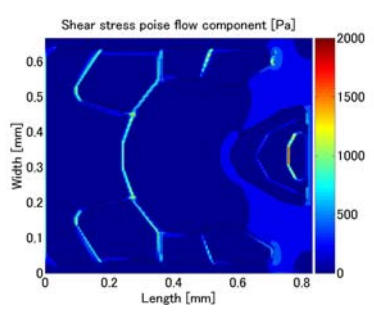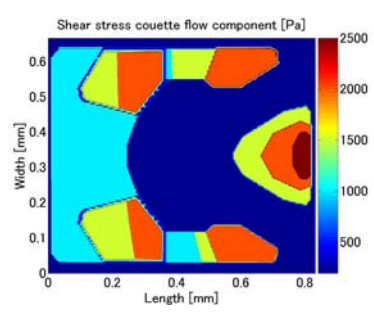

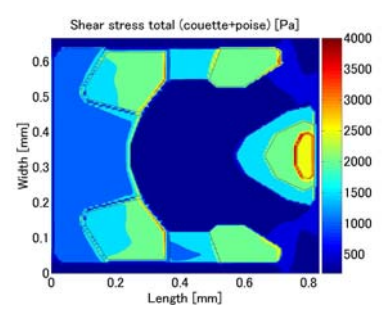
(a) slider geometry　　　(b) air bearing pressure
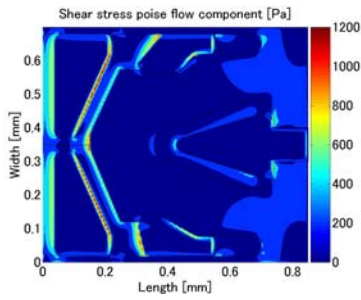
(c) air bearing shear stress
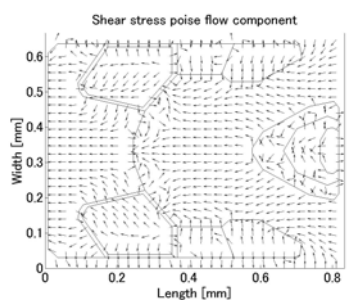
Poiseuille flow component
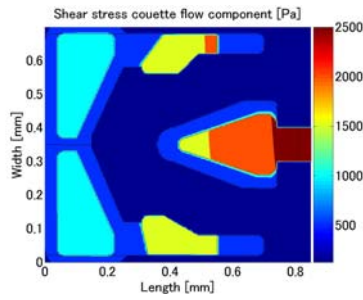


(d) air bearing shear stress
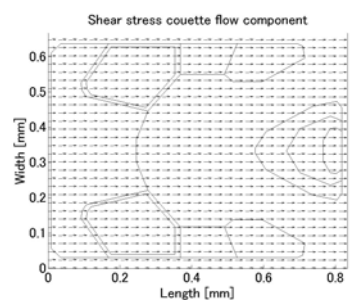
Couette flow component
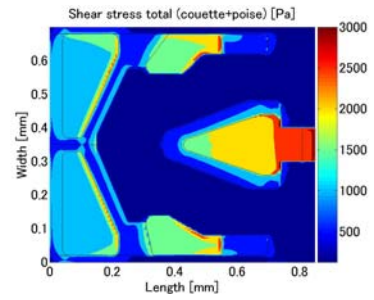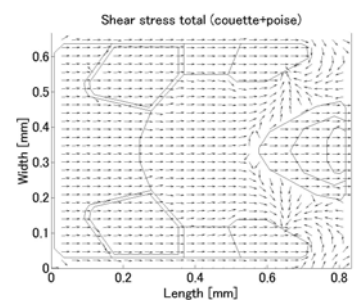


(e) total air bearing
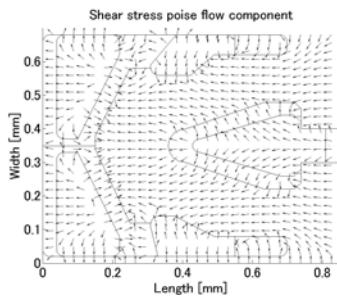
shear stress



(f) air bearing shear stress

Poiseuille flow component

direction vectors



(g) air bearing shear stress

Couette flow component

direction vectors



(h) total air bearing

shear stress direction

vectors

Figure.31 CML femto slider, slider geometry and air bearing pressure and shear stress



(a) t=0.0 [s]



(b) t=10.0 [s]



(c) t=30.0 [s]
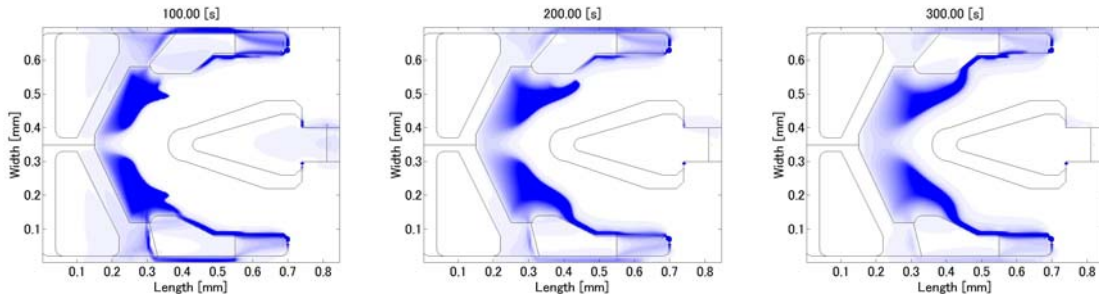
(d) t=100.0 [s]          (e) t=200.0 [s]          (f) t=300.0 [s]

Fig.32 Simulation results under CML femto slider
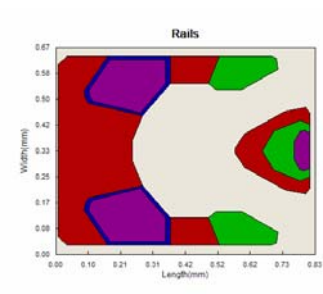
(a) slider geometry          (b) air bearing pressure
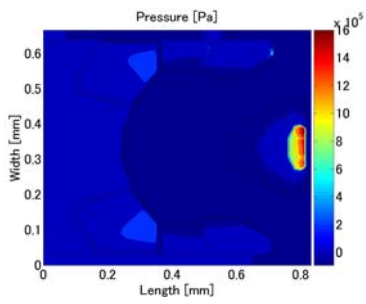


(c) air bearing shear stress     (d) air bearing shear stress      (e) total air bearing

  Poiseuille flow component       Couette flow component            shear stress



(f) air bearing shear stress     (g) air bearing shear stress      (h) total air bearing

  Poiseuille flow component       Couette flow component            shear stress direction

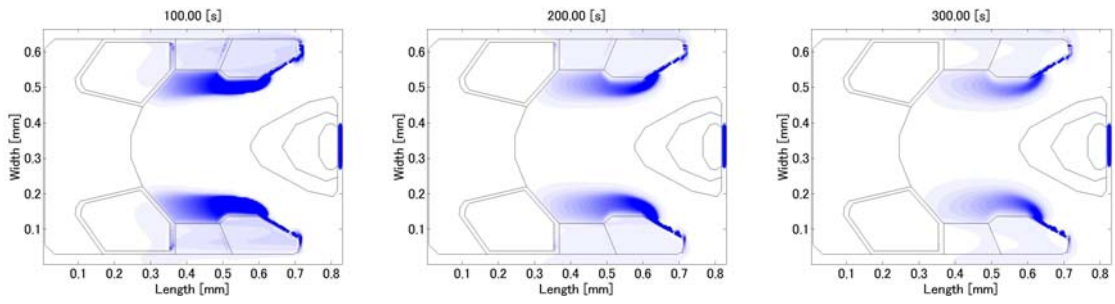  direction vectors                direction vectors                 vectors

Figure.33 DSI femto slider, slider geometry and air bearing pressure and shear stress
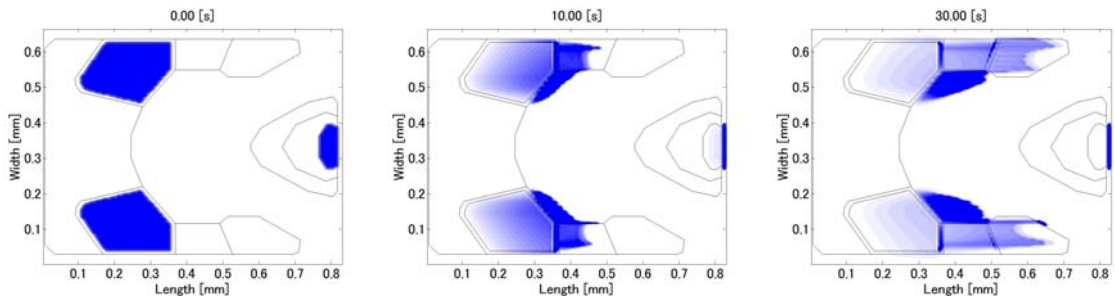
(a) t=0.0 [s]          (b) t=10.0 [s]          (c) t=30.0 [s]
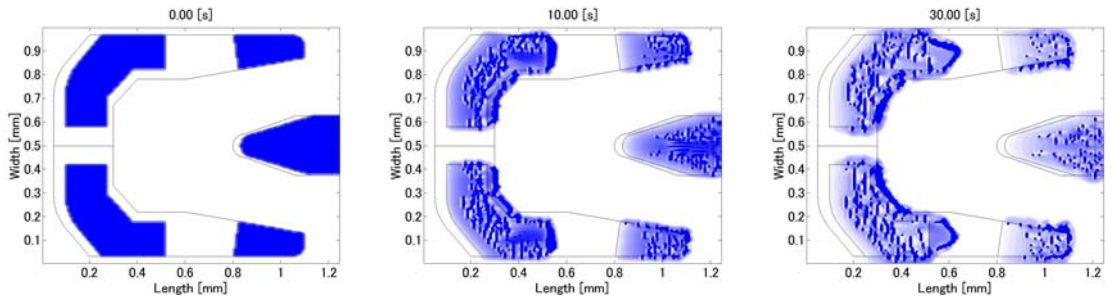
(d) t=100.0 [s]        (e) t=200.0 [s]         (f) t=300.0 [s]
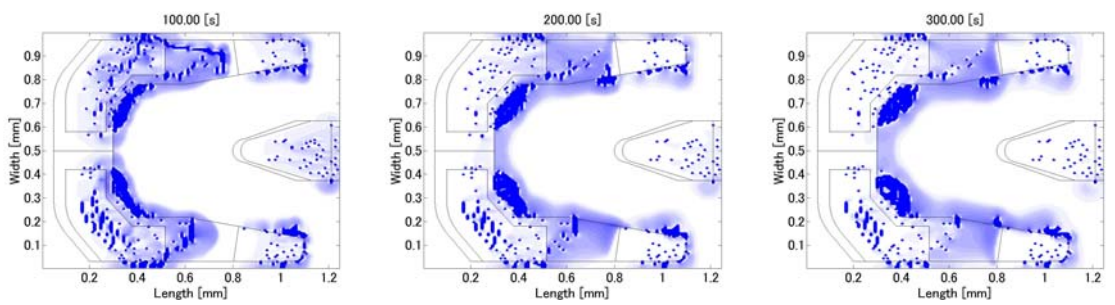
Fig.34 Simulation results under DSI femto slider



(a) t=0.0 [s]          (b) t=10.0 [s]          (c) t=30.0 [s]

(d) t=100.0 [s]                    (e) t=200.0 [s]                    (f) t=300.0 [s]

Fig.35 Simulation results under CML 7nm slider

with polar component of disjoining pressure